AFRL-RV-HA-TR-2007-1132

Generation of High Frequency P and S Wave Energy by Rock Fracture During a Buried Explosion

Charles G. Sammis

University of Southern California
Department of Earch Sciences
Los Angeles, CA 90089-0740

Final Report

10 November 2007

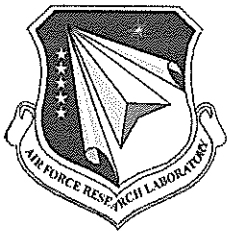

AIR FORCE RESEARCH LABORATORY
Space Vehicles Directorate
29 Randolph Road
AIR FORCE MATERIEL COMMAND
Hanscom AFB, MA 01731-3010

NOTICES

Using Government drawings, specifications, or other data included in this document for any purpose other than Government procurement does not in any way obligate the U.S. Government. The fact that the Government formulated or supplied the drawings, specifications, or other data does not license the holder or any other person or corporation; or convey any rights or permission to manufacture, use, or sell any patented invention that may relate to them.

This report was cleared for public release and is available to the general public, including foreign nationals. Qualified requestors may obtain additional copies from the Defense Technical Information Center (DTIC) (http://www.dtic.mil). All others should apply to the National Technical Information Service.

AFRL-RV-HA-TR-2007-1132 HAS BEEN REVIEWED AND IS APPROVED FOR PUBLICATION IN ACCORDANCE WITH ASSIGNED DISTRIBUTION STATEMENT.

//Signature//	//Signature//
ROBERT RAISTRICK Contract Manager	PAUL TRACY, Acting Chief Battlespace Surveillance Innovation Center

This report is published in the interest of scientific and technical information exchange, and its publication does not constitute the Government's approval or disapproval of its ideas or findings.

REPORT DOCUMENTATION PAGE [example]

Form Approved
OMB No. 0704-0188

1. REPORT DATE	**2. REPORT TYPE**	**3. DATES COVERED** *(From - To)*
10-11-2007	Final Report	08-13-2004 to 08-13-2007

Generation of High Frequency P and S Wave Energy By Rock Fracture During a Buried Explosion

5a. CONTRACT NUMBER
FA8718-04-C-0012

5b. GRANT NUMBER
N/A

5c. PROGRAM ELEMENT NUMBER
62601F

6. AUTHOR(S)
Charles G. Sammis

5d. PROJECT NUMBER
1010

5e. TASK NUMBER
SM

5f. WORK UNIT NUMBER
A1

7. PERFORMING ORGANIZATION NAME(S) AND ADDRESS(ES)

University of Southern California
Department or Earth Sciences
Los Angeles, CA 90089-0740

8. PERFORMING ORGANIZATION REPORT NUMBER

9. SPONSORING / MONITORING AGENCY NAME(S) AND ADDRESS(ES)

Air Force Research Laboratory
29 Randolph Rd.
Hanscom AFB, MA 01731-3010

10. SPONSOR/MONITOR'S ACRONYM(S)
AFRL/RVBYE

11. SPONSOR/MONITOR'S REPORT NUMBER(S)
AFRL-RV-HA-TR-2007-1132

12. DISTRIBUTION / AVAILABILITY STATEMENT

Approved for Public Release; Distribution Unlimited.

13. SUPPLEMENTARY NOTES

14. ABSTRACT
The micromechanical damage mechanics developed by Ashby and Sammis (1990) was used to explore the effects of rock fracture on the seismic coupling of explosions. An important focus was the effect of ice in the fractures. The main effect of ice in the cracks of crystalline rock is to bridge the existing cracks forming a larger number of smaller cracks. Ice also increases the coefficient of friction on the cracks resulting in a significant increase in both elastic stiffness and fracture strength, both of which are temperature and strain-rate dependent. The damage mechanics model was used to interpret laboratory data on frozen rock and a field experiment in which chemical explosions were detonated above and below the permafrost layer in Alaska to directly observe the effect of ice in rock on the seismic coupling. Finally, we used the "equivalent elastic medium model" for an explosive source developed by Johnson and Sammis (2001) to explore the effect of an increase in both elastic stiffness and compressive strength on the amplitude of far-field seismic radiation. Our conclusion is that an explosion in frozen rock should have a smaller apparent yield than the same explosion in rock at temperatures above the freezing point and that the effect should be larger in limestone than in granite.

15. SUBJECT TERMS
Nonlinear source mechanics, Damage mechanics, Seismic coupling, Frozen rock

16. SECURITY CLASSIFICATION OF:			**17. LIMITATION OF ABSTRACT**	**18. NUMBER OF PAGES**	**19a. NAME OF RESPONSIBLE PERSON**
a. REPORT	**b. ABSTRACT**	**c. THIS PAGE**			Robert Raistrick
UNCLASSIFIED	UNCLASSIFIED	UNCLASSIFIED	SAR	30	**19b. TELEPHONE NUMBER** *(include area code)* 781-377-3726

Standard Form 298 (Rev. 8-98)
Prescribed by ANSI Std. Z39.18

Table of Contents

1. Summary 1

2. Introduction 1

3. Technical Approach 2

3.1. Non-linear Regimes in the Source Region of an Underground Explosion 2

3.2. Micromechanical Damage Mechanics 3

3.3. The Damage Mechanics of Frozen Rock 6

3.4 The Effect of Ice on Seismic Radiation from an Explosion 14

3.5 Field Measurements of the Effect of Ice on Seismic Coupling: The Alaska Experiment 17

4. Results and Discussion 22

5. Conclusions 22

References 23

Figures

1. Schematic diagram of the region surrounding a contained explosion in rock: r_c is the cavity radius, r_f is the radius to which failure occurs, r_d is the radius to which new damage is created, and r_e is the elastic radius beyond which waves can be approximated as elastic. 3

2. Geometry of a penny-shaped crack of radius *a,* which is extended by wing cracks of length *l*. 4

3. Generation of fracture damage in the shock front of an underground explosion. 6

4. Strength of granite, limestone, and sandstone in uniaxial compression at low temperatures from Mellor (1973). Note that only in granite are the strengths of saturated and air-dry samples nearly the same at all temperatures. 8

5. Strength of granite, limestone, and sandstone in uniaxial tension at low temperatures from Mellor (1973). Note that the saturated samples for all three rock-types show more strengthening at low temperatures than do the air-dry samples. 8

6. Coefficient of friction on starter cracks required if the damage mechanics model is to explain the increase in compressive strength at low temperatures in Fig. 4. 9

7. Stress state for a cylindrical asperity loaded to its compressive yield stress σ_y.
Note that $\tau_y = 0.5\sigma_y$ where τ_y is the shear strength. 11

8. Plot of equation (17) in the text. The slope in the thermally activate region gives $Q/nR = 714$. At temperatures below about 110°C the mechanisms changes to glide controlled plasticity 12

9. The effect of fractures on the elastic wave velocities in wet and dry rock (from O'Connell and Budiansky, 1974). The crack density parameter ε is closely related to the damage parameter in the Ashby and Sammis (1990) damage mechanics, differing only by a constant (see eqn.20). 13

10. Deformation-mechanism map for ice. Note that increasing the strain-rate by 5 orders of magnitude near 0C increases the shear strength (effective shear stress) by a factor of 10. This increase in strength is limited by pressure melting that occurs at an effective shear stress of about 10 MPa. (From Frost and Ashby, 1982). 14

11. The effect on the radial distribution of damage when the coefficient of static friction is increased from $\mu = 0.6$ to $\mu = 1.0$ in the NPE simulation by Johnson and Sammis (2001). 15

12. The effect on the radial distribution of damage when the non-linear reference strain is increased by factors of 2 and 4 in the NPE simulation by Johnson and Sammis (2001). This is equivalent to increasing the compressive strength by a factor of 2 (simulating ice in granite) and 4 (simulating ice in limestone). 16

13. The effect of ice in the cracks on the reduced velocity potential and far-field displacement. The solid circle is the velocity potential and displacement at a radial distance of 650 m from the NPE explosion calculated by Johnson and Sammis (2001). The other symbols show the effect of changing either the initial velocity or strength of the rock. Note that effect of increasing either the initial seismic velocity or the strength is to reduce the amplitude of the seismic radiation in the far field making the explosion appear smaller than an equivalent explosion in rock above the freezing temperature of water. 17

14. Upper panel shows the location of frozen and unfrozen test sites. Lower panel shows cross-section A-A' as indicated on the upper map. 18

15. Displacement spectra for explosions in unfrozen dry schist (UN) and frozen gneiss (FR). Note the spectral peak and higher corner frequency for shots at the frozen site. (Figure courtesy of Jessie Boner at Weston Geophysical). 19

16. The ratio of saturated to dry velocities as a function of the crack parameter ε. The curves were calculated from Figure 2. The points are ratios of the ultrasonic data for schist from Table 2. Note the decrease in crack parameter as confining pressure closes cracks. 21

1. SUMMARY

The micromechanical damage mechanics formulated by Ashby and Sammis (1990) was used to explore the effect of ice in the cracks of crystalline rock on the seismic coupling of nuclear explosions detonated in the permafrost layer at arctic test sites. Experimental data show that frozen rock is elastically stiffer and has a higher fracture strength that either saturated or dry rock above the freezing point of water, and that these increases in stiffness and strength increase as temperature is decreased. The damage mechanics gave a good description of these data if the principal effect of ice in the cracks is to increase the coefficient of sliding friction. The known temperature dependence of creep in ice gave a quantitative description of the increase in strength with decreasing temperature. An important implication of this model is that the strength should also be strain-rate dependent, making it an important factor even at temperatures near the melting point of ice due to the high loading rates in the compressive front of an explosion.

The damage mechanics model was also used to help interpret the results of a field test conducted in collaboration with Weston Geophysical and New England Research. Identical chemical explosions were detonated in frozen and unfrozen schist near Fairbanks Alaska. Explosions at the frozen site produced more high-frequency energy resulting in a higher corner-frequency in the seismic spectrum and, by implication, a smaller elastic radius. This result is consistent with damage mechanics simulations in which ice in the cracks suppresses fracture damage and predicts a smaller elastic radius. In these simulations, ultrasonic velocity measurements by New England Research on frozen and unfrozen lab samples from the two sites were used, together with seismic velocities, to calculate the insitu initial damage at the frozen and unfrozen test sites.

2. INTRODUCTION

The overall objective of this research program has been to use micromechanical damage mechanics developed by Ashby and Sammis (1990) to describe the effects of the extensive fracture and granulation of rock known to occur in the non-linear source region of underground nuclear explosions. The initial objective was to explain the anomalously wide seismic pulses produced by explosions in crystalline rock that were not generated by the numerical simulations. The introduction of fracture damage into the numerical models has removed this discrepancy between theory and the observation, and the micromechanical model-based damage rheology developed by Ashby and Sammis (1990) has been built into the finite difference computer models currently used to model the seismic coupling of underground nuclear explosions (Rimer et al., 1999; Stevens et al., 2002).

One interesting consequence of having a micromechanical model for the damage is that the seismic radiation from the individual fractures can be calculated. Although the radiation from each fracture is small and very high-frequency, Johnson and Sammis (2001) found that the net effect of integrating all the fractures is the radiation of significant secondary P wave energy in the seismic band. If there is a preferred regional pre-stress direction, or if the initial damage has a preferential orientation, or both, then the damage process can also radiate significant secondary S wave energy in the seismic band. This result is relevant to the monitoring program because

recent advances in seismic discrimination and yield estimate of underground nuclear explosions have been based largely on high-frequency local phases such as L_g and higher-mode surface waves. This shift in focus to higher frequencies has stimulated new interest in understanding the non-linear seismic coupling near the source. One result of our current phase of research reported below is the direct observation of S wave generation by damage in high-speed digital photographs of laboratory explosions in photoelastic plates.

The major advantage of using a micromechanical damage model is that the effects on seismic coupling of depth of burial, ground water, and fracture patterns in the source rock can be accounted for in a physically meaningful way by modeling their effect on the nucleation, growth and interaction of fractures in the source rock. For example, the question of the effect of permafrost on seismic coupling has recently arisen. The bulk of this report details our use of the damage mechanics model to explore the effect of ice in cracks on seismic coupling in frozen crystalline rock. We first use the model to explain lab data on the effects of ice on strength and elastic stiffness of crystalline rock. We then model the results of a field experiment carried out in collaboration with Weston Geophysical and New England Research in which identical chemical explosions were detonated in frozen and un-frozen gneiss near Fairbanks Alaska.

3. TECHNICAL APPROACH

3.1 Non-linear Regimes in the Source Region of an Underground Explosion

Several different processes occur in the rock near a tamped underground explosion as illustrated in Figure 1 (see, e.g., Rodean, 1971). The explosion is initially contained within a cavity of radius r_c, which has been excavated from the surrounding rock. At the time of detonation a hot pressurized gas is created within the cavity, which causes it to expand. Some of the surrounding rock may be vaporized and added to the cavity gas at this time. The sudden expansion of the cavity generates a shock wave that propagates outward causing major damage to the surrounding rock and producing the series of regimes summarized in Figure 1. Rock first flows plastically; then is stressed beyond its brittle failure limit and becomes granulated; then is stressed to the point where radial cracks grow but failure is not reached; then deforms anelastically where pre-existing cracks slide but do not grow; and finally deforms elastically. These regimes reflect the decrease in energy density in the shock with distance from the explosion caused partly by spherical spreading and partly by the fact that energy is being used to fracture and deform the rock. The shock wave gradually decays into an inelastic wave involving non-linear motions, which further decays with distance until a radius is reached where the motions are small enough to be described by the ordinary elastodynamic equations of linear elasticity. Beyond this elastic radius, r_e, the disturbance caused by the explosion can be modeled as linear elastic waves that propagate throughout the rest of the earth.

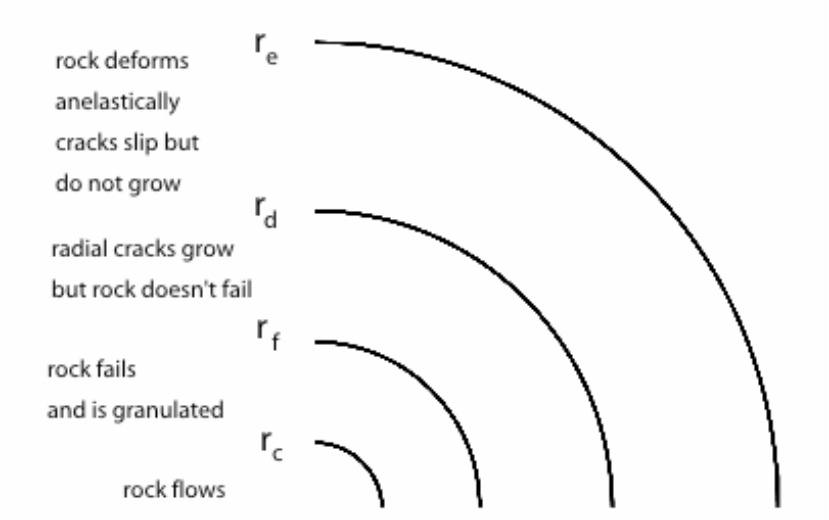

Figure 1. Schematic diagram of the region surrounding a contained explosion in rock: r_c is the cavity radius, r_f is the radius to which failure occurs, r_d is the radius to which new damage is created, and r_e is the elastic radius beyond which waves can be approximated as elastic.

These processes that occur around an explosion can have strong effects on the elastic waves that are radiated beyond the elastic radius r_e. In this report we concentrate on the growth of pre-existing cracks that can affect the radiated elastic waves in at least three different ways. First, intense cracking will significantly lower the bulk modulus and shear modulus near the source (O'Connell and Budianski, 1974; Rimer et al. 1998). Second, it has been speculated that when cracking extends into the failure regime, acoustic fluidization can lower the basic strength of the rock (Sammis, 1998). Third, motions on the cracks serve as secondary sources of elastic waves that can contribute to the net seismic radiation field.

The spatial extent of each regime and the associated mechanics are calculated using the formulation of Ashby and Sammis (1990) to model the nucleation and growth of cracks in the source region, which is here referred to as damage. Calculation of this damage requires knowledge of the stress field in the region surrounding the source, which is approximated in this study by the equivalent elastic method (Johnson, 1993; Johnson and Sammis, 2001).

3.2 Micromechanical Damage Mechanics

The concept of damage used here is that developed by Ashby and Sammis (1990). In that paper, the conditions under which an initial crack can nucleate additional cracking are derived. Only the basic equations needed to calculate the increase in damage at the shock front will be repeated here. In 3D the initial damage is defined as

$$D_0 = \tfrac{4}{3}\pi\left(a\cos\chi\right)^3 N_V, \qquad (1)$$

where a is the radius of penny-shaped cracks, χ is angle describing the orientation of the cracks (see Figure. 2) and N_V is the number of cracks per unit volume. In response to loading, wing cracks of length l grow at opposite edges of the initial crack thereby increasing the damage to

$$D = \frac{4}{3}\pi\left(l + a\cos\chi\right)^3 N_V . \tag{2}$$

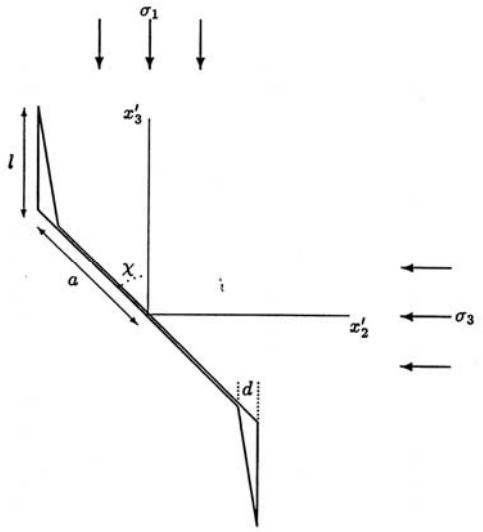

Figure 2. Geometry of a penny-shaped crack of radius a, which is extended by wing cracks of length l.

The value of l is determined by letting the wing cracks grow until the stress intensity factor at the tip decreases to the fracture toughness of the medium. The equation that must be solved to determine the final amount of damage is (Ashby and Sammis, 1990)

$$S_1 = -\frac{C_2\left(\left(\frac{D}{D_0}\right)^{1/3} - 1 + \frac{\beta}{\cos\chi}\right)^{2/3} - S_3\left[C_1\left(1 + \left(\frac{C_3 D_0^{2/3}}{1-D^{2/3}}\right)\left(\left(\frac{D}{D_0}\right)^{1/3} - 1\right)^2\right) + C_4\left(\left(\frac{D}{D_0}\right)^{1/3} - 1\right)^2\right]}{1 + \frac{C_3 D_0^{2/3}}{1-D^{2/3}}\left(\left(\frac{D}{D_0}\right)^{1/3} - 1\right)^2} \tag{3}$$

Here S_1 and S_3 are the maximum and minimum normalized principal compressive stresses given by

$$S_1 = \frac{\sigma_1}{K_{Ic}/\sqrt{\pi a}}, \qquad S_3 = \frac{\sigma_3}{K_{Ic}/\sqrt{\pi a}} \tag{4}$$

and K_{Ic} is the critical stress intensity for mode I cracks, a material property. The constants in (3) are

$$
\begin{aligned}
C_1 &= \frac{\left(1+\mu^2\right)^{1/2}+\mu}{\left(1+\mu^2\right)^{1/2}-\mu} \\
C_2 &= \pi(\cos\chi)^{3/2}\sqrt{3/\beta}\,\frac{1}{\left(1+\mu^2\right)^{1/2}-\mu} \\
C_3 &= 2 \\
C_4 &= 2\pi(\cos\chi)^{2}\sqrt{3/\beta}\,\frac{1}{\left(1+\mu^2\right)^{1/2}-\mu}
\end{aligned}
\qquad (5)
$$

In these last equations, μ is the coefficient of static friction and β is a correction factor for the effective length of the crack, typically 0.45 introduced by Ashby and Sammis (1990) to bring their approximate analytical model into agreement with numerical simulations in the limit of small l. Also, χ is assumed here to be 45°.

Given the initial damage D_0 and the principal stresses σ_1 and σ_3, equation (3) can be used to calculate the equilibrium state of damage. This is a cubic equation in the damage, which we solve numerically. There are three possible outcomes. At low stresses, wing cracks do not nucleate and we get no real solutions. At intermediate stresses we calculate a value of $D>D_0$ until a maximum is reached above which we again get no real solutions. Ashby and Sammis (1990) interpret this maximum as failure since, for additional loading, damage increases at decreasing stress, an unstable condition leading to shear localization. We do not attempt to model this post-failure regime beyond identifying it as the granulated region described in the previous section, and as a possible site for further weakening by acoustic fluidization. Figure 3 shows a conceptual model of how damage is generated in the stress field at the shock front of the explosion. In this case the principal stresses are the radial and hoop stress in the spherical geometry.

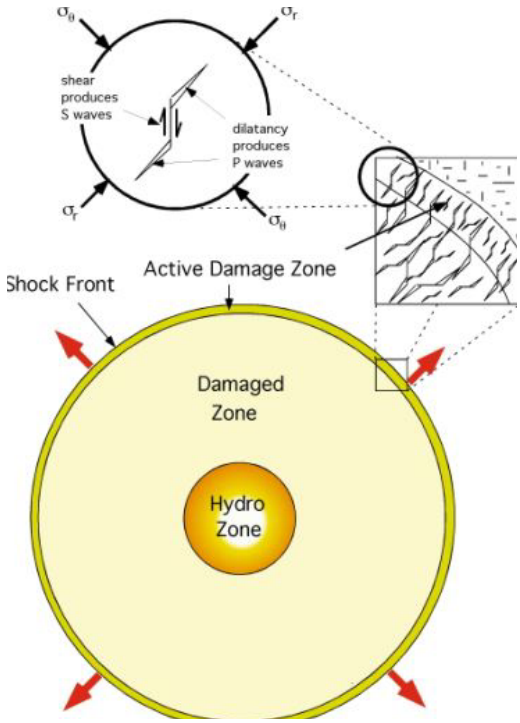

Figure 3. Generation of fracture damage in the shock front of an underground explosion.

3.3 The Damage Mechanics of Frozen Rock

Uniaxial compressive and tensile tests at low temperature have shown that freezing can increase rock strength by a factor of 4 in porous rock and by a factor of 1.8 in crystalline rock (Mellor, 1973). We now interpret these data using the micromechanical damage model developed by Ashby and Sammis (1990) in which sliding on preexisting cracks in rock induces additional fracture damage and ultimate failure. The effect of ice in this model is to increase the effective coefficient of sliding friction on the preexisting cracks thus inhibiting the generation of new damage and strengthening the rock. In addition to strengthening, the damage model is also able to explain some of the subtler phenomenology in the ice data such as the differences between porous and crystalline rock and the progressive strengthening observed to occur as the temperature is lowered from 0°C to −150°C.

The strengthening associated with low temperatures can be expected to significantly reduce the apparent radius of an explosion by suppressing crack growth in the non-linear damage zone, thus producing a higher frequency seismic signature than that from an equivalent explosion in rock above 0°C. Also, the "pulse broadening" phenomena observed for shots in crystalline rock, which has been associated with dynamical weakening of the damage zone, should be suppressed in frozen crystalline rock.

3.3.1 The Uniaxial Strength of Frozen Rock

Mellor (1973) measured the uniaxial compressive and tensile strength of granite, limestone, and sandstone over a temperature range from $20°C$ to $-197°C$ for both water saturated and air-dry samples. Results from the compressive tests are shown in Fig.4 and those from the tensile tests in Fig. 5. We first make a few observations about these results and offer a qualitative explanation of each in terms of the damage mechanics model. A more quantitative model for the granite data is given in the next section.

Observation 1: In compression, the saturated samples for all three rock-types show a strong increase in strength beginning at $0°C$ and continuing to $-120°C$. The air-dry limestone and sandstone samples do not show a comparable increase in strength at low temperatures. However, both the air-dry and saturated granite samples strengthen at approximately the same rate with decreasing temperature.

Damage Mechanics Explanation: In the saturated samples for all three rock-types, frozen water inhibits sliding on the preexisting flaws, suppressing damage and strengthening the samples. The flow strength of ice increases as the temperature falls below the freezing point thus increasing the apparent coefficient of friction and strengthening the samples. For the air-dry limestone and sandstone specimens, there is not enough adsorbed water in the pores to provide this strengthening. However, for granite the preexisting microcracks are much narrower. The adsorbed water in the air-dry samples effectively saturates these cracks, and hence there is little difference between the low temperature compressive strength of saturated and air-dry granite. Note that the saturated granite is significantly weaker at $20°C$. This may be due to hydrolytic weakening which is suppressed below $0°C$.

Observation 2: In tension, the saturated samples again all show an increase in strength beginning at $0°C$ and increasing to lower temperatures. However, in tension, none of the air-dry samples showed a comparable increase in strength. Even the air-dry granite samples remain significantly weaker than the saturated ones at low temperature.

Damage Mechanics Explanation: Failure in tension is nucleated at the largest most dangerously oriented flaw, which grows unstably to produce macroscopic failure. Failure in compression is a cooperative phenomenon involving structures created by the interaction of a myriad of smaller flaws. The reason that the tensile strength in air-dry granite does not track that of the saturated granite, is that the largest crack (the one responsible for the tensile failure) is too large to be saturated by the films of adsorbed water that saturate the myriad of smaller microcracks responsible for compressive failure.

We now quantify these observations by including the effect of frozen water in the Ashby and Sammis (1990) damage mechanics model for granite.

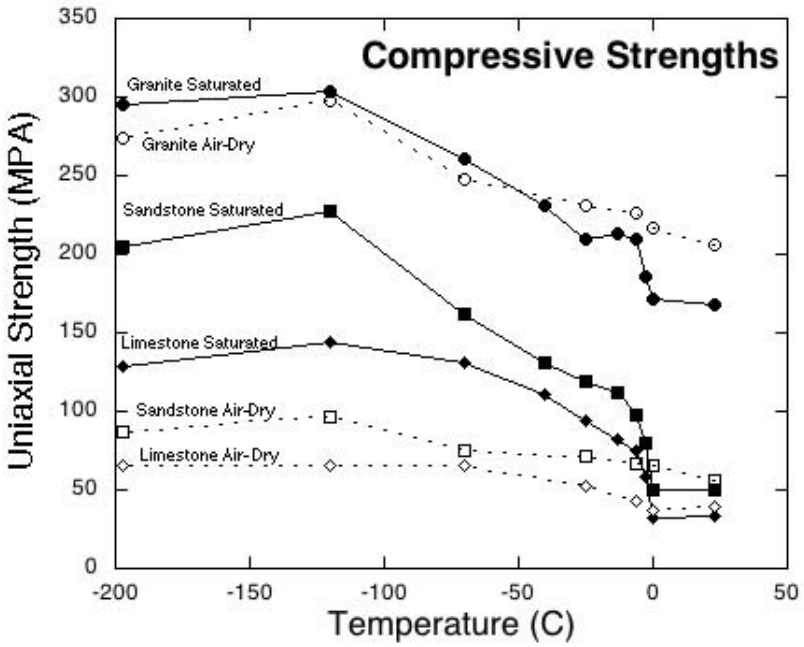

Figure 4. Strength of granite, limestone, and sandstone in uniaxial compression at low temperatures from Mellor (1973). Note that only in granite are the strengths of saturated and air-dry samples nearly the same at all temperatures.

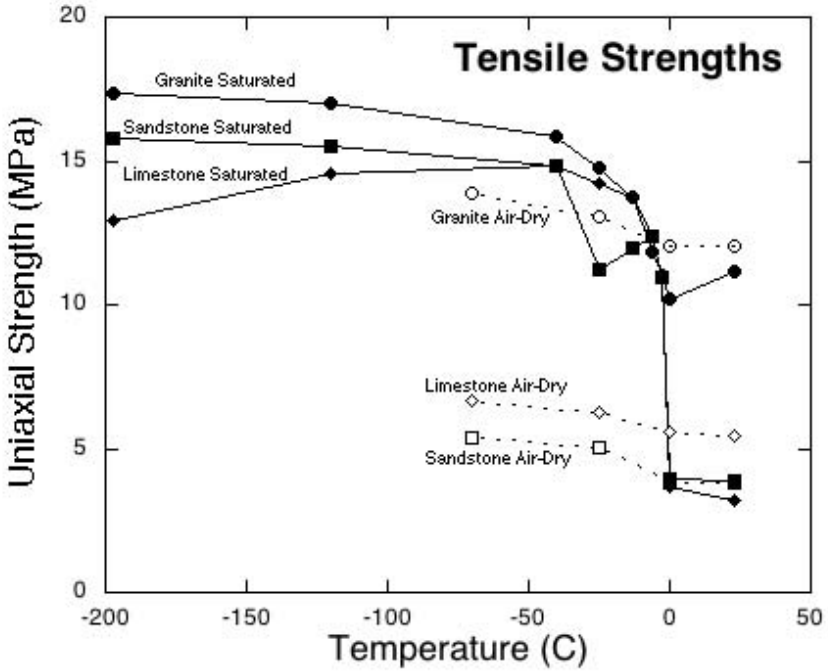

Figure 5. Strength of granite, limestone, and sandstone in uniaxial tension at low temperatures from Mellor (1973). Note that the saturated samples for all three rock-types show more strengthening at low temperatures than do the air-dry samples.

3.3.2 A Damage Mechanics Model for the Strength of Frozen Granite

Ashby and Sammis (1990) show that an initial inclined crack will nucleate tensile wing cracks (as illustrated in Fig. 2) when

$$S_1 = C_1 S_3 + S_o \qquad (6)$$

where S_1 and S_3 are given in eqn. (4).

Using the published value for the critical stress intensity factor $K_{Ic} = 1$ MPa m$^{1/2}$, Ashby and Sammis (1990) fit eqn. (6) to data for the initiation of microcrack damage in granite to determine μ in the range 0.55 to 0.65 and a crack length 2a near 1 mm. The assumption is that the cracks do not interact during nucleation so that eqn. (6) is independent of the initial crack density D_o.

The failure curve is sensitive to the intial crack density, which (in 3D) is expressed by the initial damage D_o defined in eqn. (1). When eqn. (3) is used to plot S_1 as a function of D (for fixed values of D_o, S_3 and the other parameters), S_1 has a maximum value which Ashby and Sammis (1990) interpret as the failure stress. For larger values of D beyond this peak, S_1 decreases. This weakening rheology leads to shear localization and macroscopic failure. Fitting the uniaxial strength of dry granite at 20°C using the values of a and μ deduced above from the nucleation gives an initial damage of $D_o = 0.1$.

We now ask how much of an increase in μ is required to produce the compressive strengthening at low temperatures observed in Fig. (4). Holding all the other parameters constant, we increased μ to get the uniaxial strength measured by Mellor (1973) (Fig.4). Figure 6 shows the value of μ as a function of temperature required by this damage mechanics interpretation of Mellor's (1973) data.

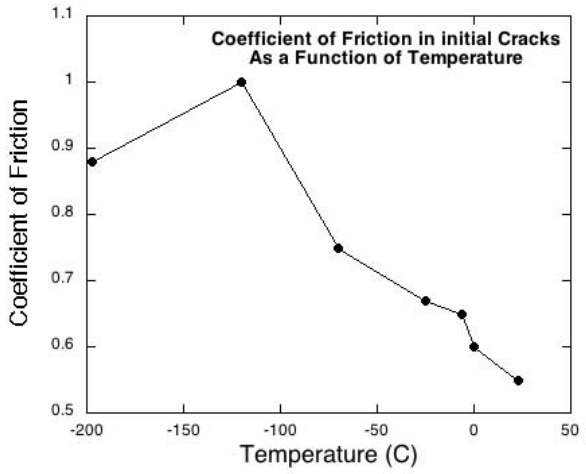

Figure 6. Coefficient of friction on starter cracks required if the damage mechanics model is to explain the increase in compressive strength at low temperatures in Fig. 4.

3.3.3 The Apparent Coefficient of Friction of Frozen Cracks

The coefficient of friction μ is defined by Amonton's Law that relates the shear stress τ required to initiate sliding between two surfaces that are supporting a normal stress $\tilde{\sigma}$

$$\tau = \mu\sigma \tag{7}$$

In the case where the boundary contains a fluid with pressure *P*, friction is described by the apparent friction law

$$\tau = \mu(\sigma - P) \tag{8}$$

The coefficient of friction shows the smallest variation across different rock types of any mechanical parameter. Known as "Byerlee's Law", $\mu \approx 0.6$ for virtually all rock surfaces independent of hardness.

The asperity model for friction, initially formulated by Bowden and Tabor (1950, 1964) offers a simple physical explanation for the constancy of μ. This model recognizes that all surfaces are rough at some scale, and that actual contact occurs at a limited number of high points called asperities. Under a normal load σ the asperities flow thereby increasing the true area of contact, A_c, until the stress on the asperities falls to the normal yield stress, σ_y, of the rock. If the apparent area of the contacting surfaces is *A*, we have

$$\sigma A = \sigma_y A_c \tag{9}$$

The shear stress τ required to initiate sliding is determined by the shear yield stress τ_y at which the asperities fail in shear, which gives:

$$\tau A = \tau_y A_c \tag{10}$$

Equations (9) and (10) may be combined to write

$$\tau = \left(\frac{\tau_y}{\sigma_y}\right)\sigma, \tag{11}$$

which is just Amonton's law where $\mu = \tau_y / \sigma_y$.

To see why the ratio τ_y / σ_y is nearly independent of rock type, consider the strength of a single asperity with cross-section A_c that is loaded to the compressive yield stress σ_y. This asperity will fail when the maximum shear stress reaches τ_y. As illustrated by the Mohr Circle in Fig. 7

the normal yield stress is related to the shear yield stress by $\tau_y / \sigma_y = 0.5$, independent of the material.

If the area between the asperities is saturated with water, this will have no direct effect on μ, as long as P<=0. However, if this water freezes, the shear resistance will increase to

$$\tau = \tau_{y_{rock}} \frac{A_{c_{rock}}}{A} + \tau_{y_{ice}} \frac{A_{c_{ice}}}{A} \tag{12}$$

Assuming that the normal load is supported entirely by the rock asperities such that

$$\sigma = \sigma_{y_{rock}} \frac{A_{c_{rock}}}{A} \tag{13}$$

we can express the ice strengthening by an apparent coefficient of friction μ' as

$$\mu' = \frac{\tau}{\sigma} = \frac{\tau_{y_{rock}} A_{c_{rock}} + \tau_{y_{ice}} A_{c_{ice}}}{\sigma_{y_{rock}} A_{c_{rock}}} = \mu + \frac{\tau_{y_{ice}}}{\sigma_{y_{rock}}} \frac{A_{c_{ice}}}{A_{c_{rock}}} \tag{14}$$

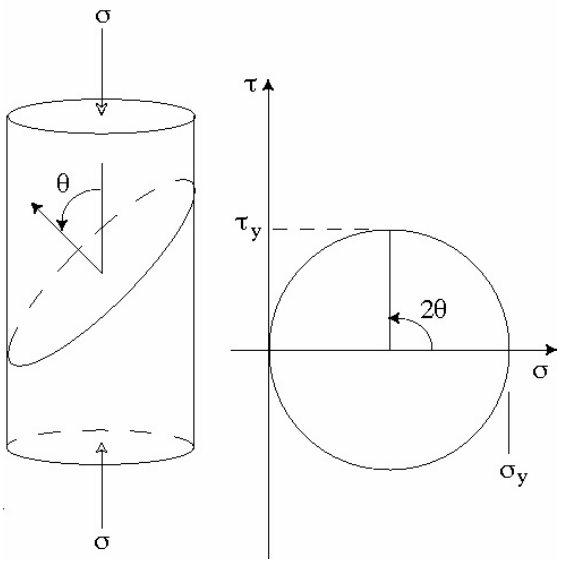

Figure 7. Stress state for a cylindrical asperity loaded to its compressive yield stress σ_y. Note that $\tau_y = 0.5\sigma_y$ where τ_y is the shear strength.

Direct observation of asperities on surfaces of transparent silicates has shown that they deform by plastic flow during shear (Dieterich and Kilgore, 1996). At the high stresses and low homologous temperature (T/T_m where T_m is the melting temperature) in the rock asperities, the flow stress is nearly independent of strain-rate or temperature. However, the flow stress in ice near its melting temperature is determined by thermally activated diffusion limited creep

mechanisms that are very sensitive to both temperature and strain-rate. This is why μ rises rapidly at temperatures just below $0°\text{C}$ in Fig. 6. In equation (14), this behavior is caused by the rapid increase in $\tau_{y_{ice}}$ with falling temperature below $0°\text{C}$. At very low temperatures, flow in the ice will also be controlled by glide and μ' will be almost independent of temperature and strain-rate.

Flow in ice near its melting point is more complicated than high temperature flow in rock. There is a poorly understood change in activation energy at about $-10°\text{C}$ thought to be associated with the suppression of pressure melting at grain boundaries below this temperature (Goodman et al., 1981; Duval et al., 1983). We will take the analysis in this paper one step further by assuming a generic form for this high temperature power-law flow in ice, the strain rate $\dot{\varepsilon}$ is given by

$$\dot{\varepsilon} = B\tau^n \exp(-Q/RT) \tag{15}$$

Solving for the flow stress gives

$$\tau_{y_{ice}} = \left(\frac{\dot{\varepsilon}}{B}\right)^{1/n} \exp(Q/nRT) \tag{16}$$

Using this in eqn. (14) and combining constants gives

$$\mu' = \mu + D\exp(Q/nRT) \tag{17}$$

or, equivalently,

$$\ln(\mu' - \mu) = \ln D + Q/nRT \tag{18}$$

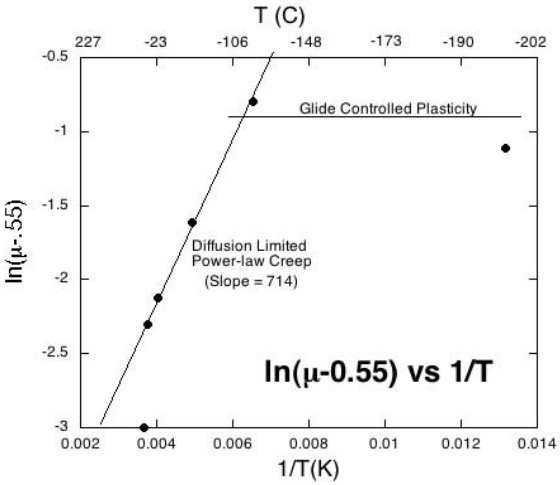

Figure 8. Plot of equation (17) in the text. The slope in the thermally activate region gives $Q/nR = 714$. At temperatures below about 110°C the mechanisms changes to glide controlled plasticity.

In Fig.8, $\ln(\mu'-\mu)$ is plotted as a function of $1/T$. The linear portion has a slope of $Q/nR = 714$. Below 8.3°C, the activation energy for power law creep is $Q \approx 80$ KJ mole^{-1}(Goodman et al., 1981). This implies a creep power of

$$n = \frac{8x10^4}{(714)(8.3)} = 13.5 \tag{19}$$

This is significantly higher than $n \approx 3$ observed at stresses below 1MPa. However, n for ice is observed to rise rapidly at stresses above 1 MPa (Goodman et al., 1981), so this may simply reflect a higher flow stress on the asperities.

3.3.4 The Effect of Ice on the Elastic Properties of Frozen Rock

The effect of ice in the inclined crack in Fig. 2 is to either totally immobilize it, thus reducing N_V in eqn. (1), or, if saturation is not total, to form ice bridges thus reducing a in eqn. (1) while increasing N_V. The net effect of both is to reduce the initial damage D_o.

The elastic moduli of rock are extremely sensitive to D_o. Figure 9, from O'Connell and Budiansky (1974) shows the effect of changing D_o on the P and S wave velocities in dry and water saturated rock. Note that the x-axis in Fig.9 is $\varepsilon = N\left\langle a^3 \right\rangle$ where N is the number of cracks per unit volume and a is the half-length of the crack. Comparison with eqn. (1) shows that ε can be written in terms of the initial damage as

$$\varepsilon = \frac{3}{4\pi}\left(\frac{1}{\cos\chi}\right)^3 D_o \approx 0.68 D_o \tag{20}$$

The effect of freezing water in the cracks is to move to the left (toward lower damage) on the curves in Fig.9. This will produce an increase in elastic wave velocity. The effect is larger for S waves than for P waves in saturated rock.

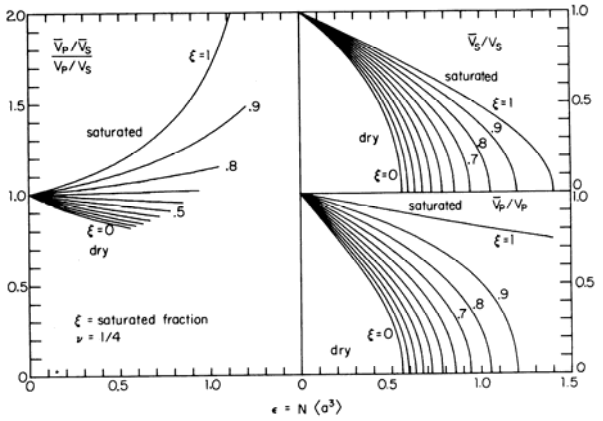

Figure 9. The effect of fractures on the elastic wave velocities in wet and dry rock (from O'Connell and Budiansky, 1974). The crack density parameter ε is closely related to the damage parameter in the Ashby and Sammis (1990) damage mechanics, differing only by a constant (see eqn.20).

3.3.5 The Effect of Strain-rate on the Strength of Frozen Rock

The effect of strain-rate on the strength of frozen rock is illustrated by the deformation-mechanism map for ice in Fig.10. Temperatures near melting are at the right edge of the map where it can be seen that increasing the strain rate produces a significant increase in the flow stress. At an effective shear stress of about 10 MPa this trend is reversed by the onset of pressure melting which weakens the ice.

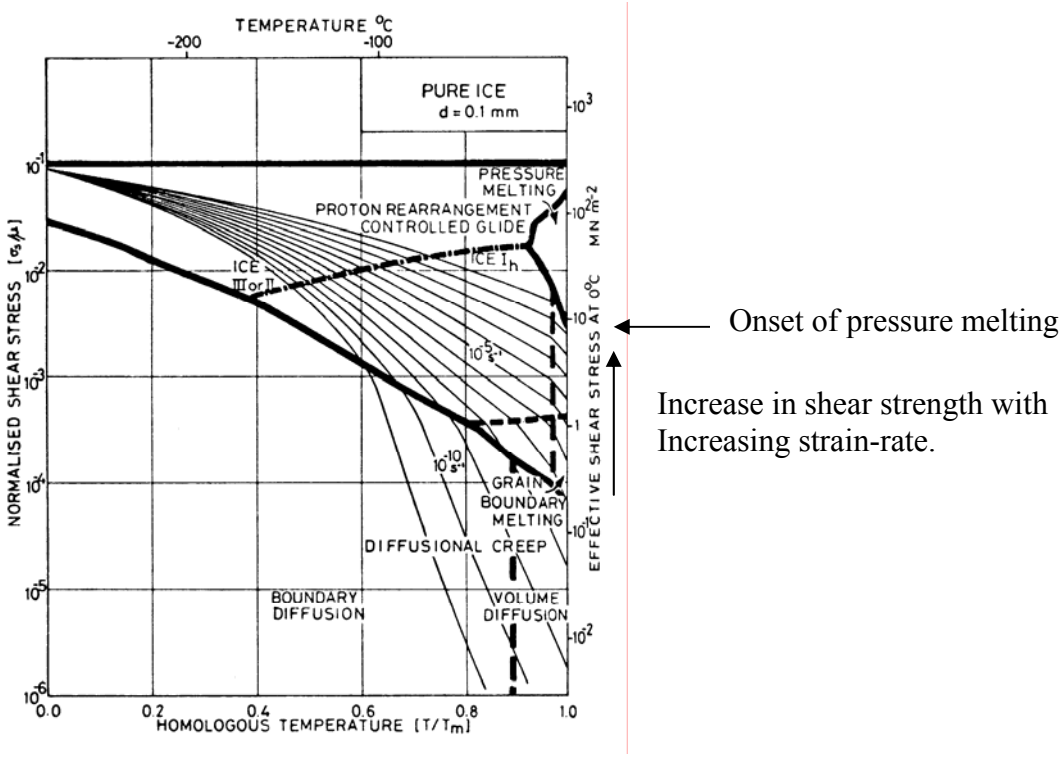

Figure 10. Deformation-mechanism map for ice. Note that increasing the strain-rate by 5 orders of magnitude near 0C increases the shear strength (effective shear stress) by a factor of 10. This increase in strength is limited by pressure melting that occurs at an effective shear stress of about 10 MPa. (From Frost and Ashby, 1982).

3.4 The Effect of Ice in Rock on Seismic Radiation from an Explosion

In order to model the effect of ice on the damage generated by an explosion and on the seismic radiation, we require the principal stresses generated by the explosion as a function of distance and time. This is made difficult by the existence of the nonlinear processes between the cavity radius and the effective elastic radius, beyond which the assumptions of ordinary linear elasticity are valid. Sophisticated computer codes have been developed which include hydrodynamic effects, shock waves, and nonlinear equations of state (see, for example, Rodean, 1971; King et al., 1989; Glenn, 1993; Glenn and Goldstein, 1994, for discussion and further references). We use here an approximate method to calculate the stresses surrounding an explosion that is based on the equivalent elastic method developed by earthquake engineers to model the nonlinear

behavior of soils that that occurs during strong ground motion. The central idea is to make the material properties a function of the stress in the outward propagating pressure pulse and then to adjust these material properties in an iterative process until the appropriate values are present at all distances from the source. In effect, the nonlinear stress-strain behavior is approximated by a series of linear relationships that change with the level of stress. The present formulation, described by Johnson (1993), relates density and bulk elastic properties to the peak pressure and shear and anelastic properties to the maximum shear strain.

The details of this model are published in Johnson and Sammis (2001) and will not be repeated here.

In Johnson and Sammis (2001) we modeled the 1 kt chemical explosion detonated in September 1993 as part of the Non-Proliferation Experiment (NPE) (see Denny, 1994) and found that the equivalent elastic model gave a good representation of the near field amplitudes. We now ask how these results would change if we increased the P and S wave velocities, the coefficient of friction, and the strength to simulate the mechanical properties if the cracks were filled with ice.

Figure 11 shows the effect on the radial distribution of fracture damage in the non-linear source region when the coefficient of friction is increased from μ=0.6 to μ=1.0. For the higher coefficient of friction, damage is suppressed close in and enhanced further out. This is because the stresses do not fall off as fast with distance due to the smaller damage close in. Radial cracks are thus expected to extend out an additional 10 meters in the frozen rock (about an additional 20%).

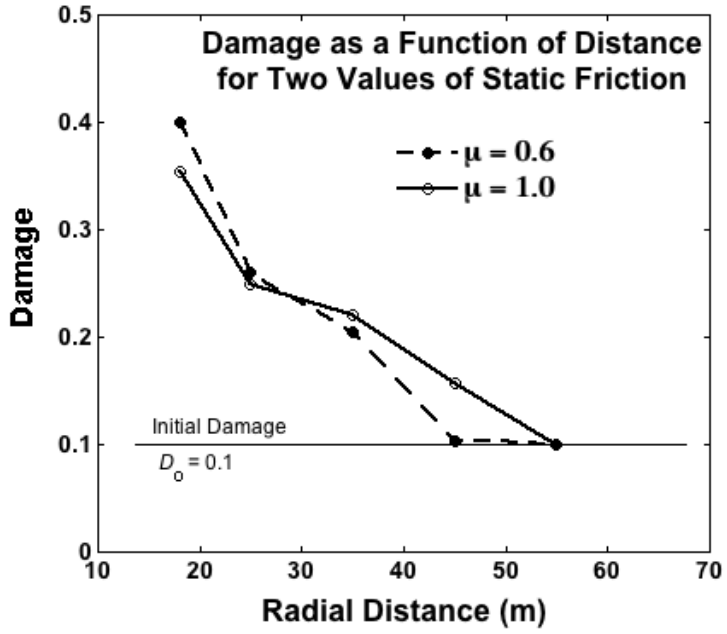

Figure 11. The effect on the radial distribution of damage when the coefficient of static friction is increased from $\mu = 0.6$ to $\mu = 1.0$ in the NPE simulation by Johnson and Sammis (2001).

Figure 12 shows the effect of increasing the compressive strength on the radial distribution of damage. In the equivalent elastic source model the compressive strength is expressed as a reference strain defined as

$$\varepsilon_r = \frac{\tau_{\max}}{\mu_o} \tag{21}$$

In Fig. 12, the reference strain is doubled (corresponding to ice in granite) and multiplied by 4 (corresponding to ice in limestone). The effect is very similar to that of increasing the coefficient of static friction – there is more damage and it extends an additional 10 meters.

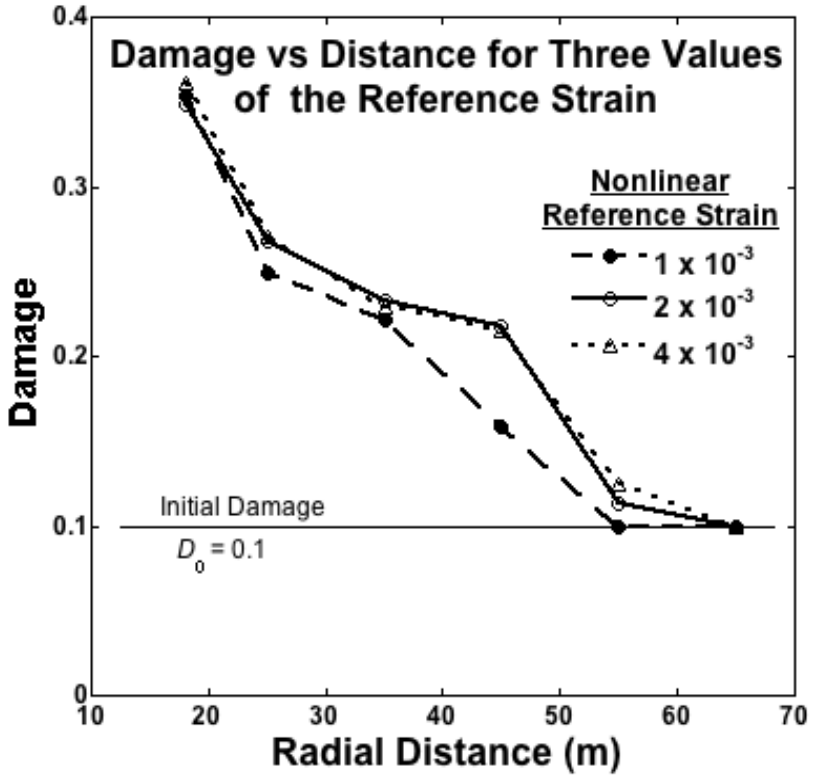

Figure 12. The effect on the radial distribution of damage when the non-linear reference strain is increased by factors of 2 and 4 in the NPE simulation by Johnson and Sammis (2001). This is equivalent to increasing the compressive strength by a factor of 2 (simulating ice in granite) and 4 (simulating ice in limestone).

Figure 13 summarizes the effect of ice in the cracks on the amplitude of seismic radiation in the far-field. As argued above, ice is expected to increase the initial wave velocities and the strength of the source rock. These ice-induced changes all decrease both the amplitude and reduced velocity potential in the linear elastic regime.

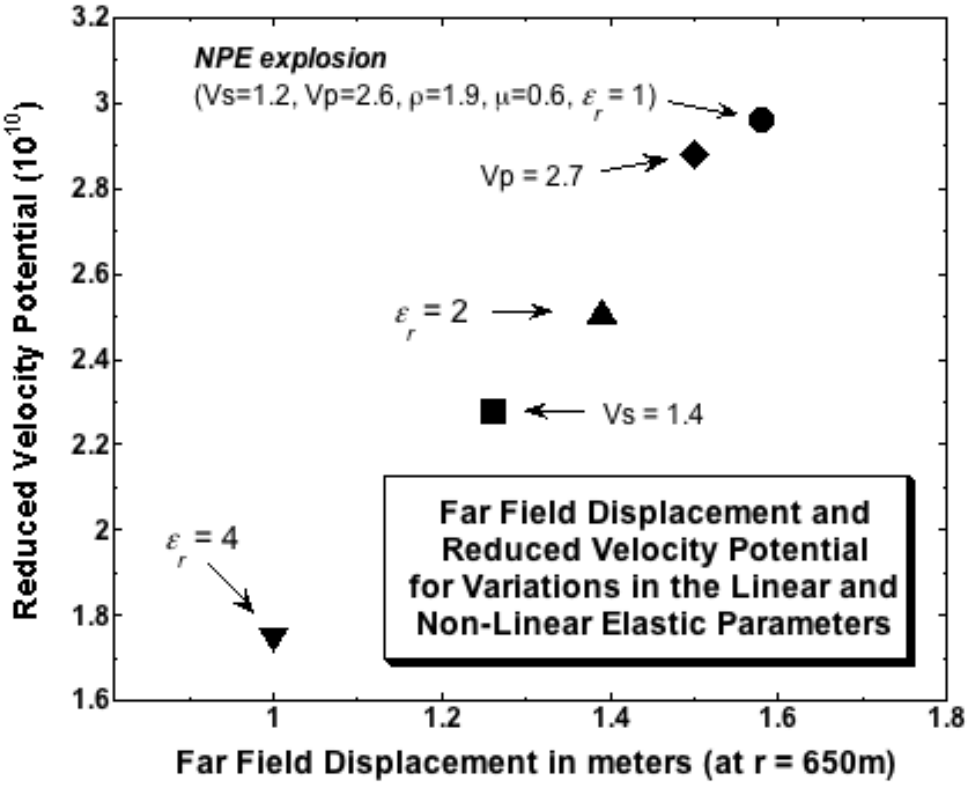

Figure 13 The effect of ice in the cracks on the reduced velocity potential and far-field displacement. The solid circle is the velocity potential and displacement at a radial distance of 650 m from the NPE explosion calculated by Johnson and Sammis (2001). The other symbols show the effect of changing either the initial velocity or strength of the rock. Note that effect of increasing either the initial seismic velocity or the strength is to reduce the amplitude of the seismic radiation in the far field making the explosion appear smaller than an equivalent explosion in rock above the freezing temperature of water.

3.5 Field Measurements of the Effect of Ice on Seismic Coupling: The Alaska Experiment

In collaboration with Weston Geophysical and New England Research a series of identical chemical explosions were detonated above and below the permafrost layer in crystalline bedrock at a site near Fairbanks Alaska (Fig. 14). The details of this experiment are given in Bonner et al. [2007]. Results summarized here include source spectra for several explosions at both sites and the seismic P and S velocities at each. Ultrasonic P and S wave velocities in laboratory samples from each test site are presented here to supplement these field data. The primary result, shown in Figure 15, was that the spectral levels of radiation from both sites were comparable, but the

corner frequency of radiation from the frozen rock site was higher. This higher corner frequency would lead to the erroneous conclusion that the explosion in frozen-rock was smaller.

The two test sites are shown on the map (Fig. 14a) and cross-section (Fig. 14b). The first, hereafter referred to as the "dry site", was located above the water table in a mica schist. The second, hereafter referred to as the "frozen site", was located below the permafrost in a gneiss. Details of the seismic instrumentation and deployment are given in Bonner et al. [2007]. Measurement of the seismic velocities at the dry site gave v_P = 2,600 m/s and v_S = 1,600 m/s, while measurements at the frozen site gave v_P = 3,600 m/s and v_S = 2,200 m/s. The yield and depth of burial of each shot are summarized in Table 1.

Table 1. Location, yield, and depth of burial of explosions near Fairbanks Alaska

Shot Number	Lat	Long	Elev (m)	Date	Origin Time	Yield (lbs)	Centroid (ft)
1	N64.94657	W147.69580	203	Aug24	17:12:36.4	200	23
2	N64.94655	W147.69603	191	Aug24	18:24:54.66	350	23
3	N64.94027	W147.71993	218	Aug24	22:13:41.81	359	35
4	N64.95389	W147.67982	353	Aug26	21:13:28.53	200	23
5	N64.95386	W147.67992	359	Aug26	22:32:52.73	350	23
6	N64.95404	W147.67966	354	Aug26	23:30:38.61	100	25
ACOU1	N64.94040	W147.71807	205	Aug24	Within 30 minutes after Shot 3	0.14	On Surface

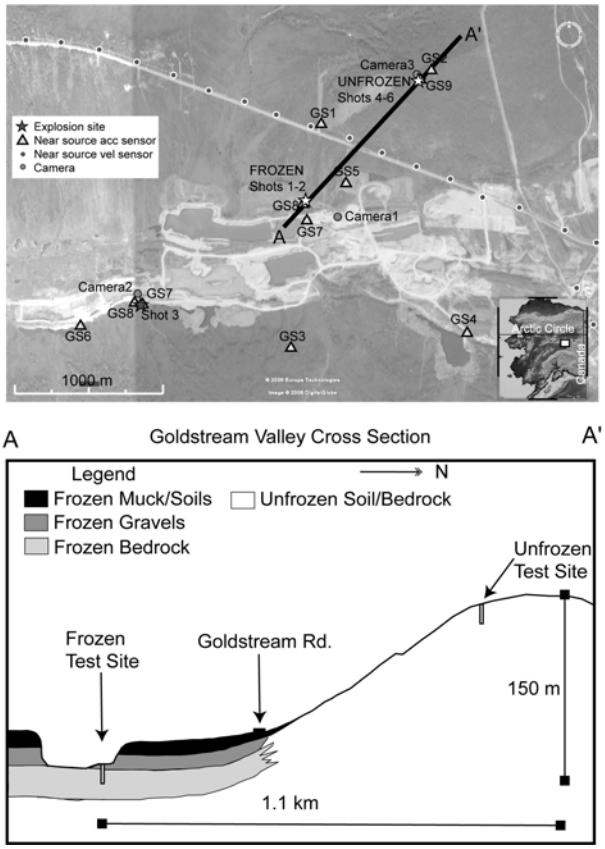

Figure 14. Upper panel shows the location of frozen and unfrozen test sites. Lower panel shows cross-section A-A' as indicated on the upper map.

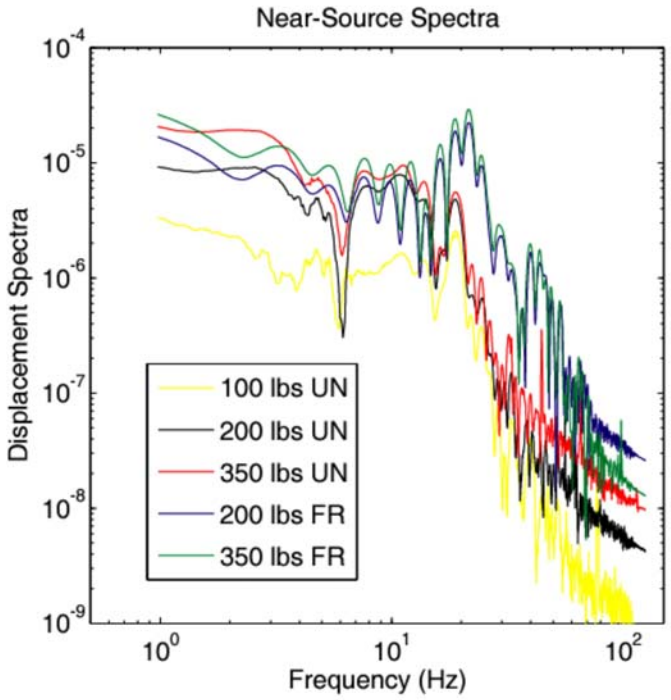

Figure 15. Displacement spectra for explosions in unfrozen dry schist (UN) and frozen gneiss (FR). Note the spectral peak and higher corner frequency for shots at the frozen site. (Figure courtesy of Jessie Boner at Weston Geophysical).

In order to make a quantitative interpretation of this result, we wish to model the Alaska explosions using the Johnson and Sammis (2001) source model. This model incorporates the Ashby and Sammis (1990) micromechanical damage mechanics, which as shown above, gives a good description experimental data for the temperature dependence of strength in frozen crystalline rock (Sammis and Biegel, 2004, 2005). The basic idea is that ice in the cracks strengthens the rock and increases its elastic stiffness by reducing the initial damage D_o. In our source model, this results in less explosion-induced damage in the frozen rock, and a higher corner frequency – as observed.

We use the theory developed by O'Connell and Budiansky (1974) to estimate D_o from the seismic velocities measured by Weston Geophysical at each field site. Figure 9 above shows the ratios $\bar{v}_P/v_P$ and $\bar{v}_S/v_S$ as functions of a crack density parameter, which they define as $\varepsilon = N_V \langle a \rangle^3$ and which is simply related to D_o in equation (20) .The quantities $\bar{v}_P$ and $\bar{v}_S$ are velocities in the fractured rock, while v_P and v_S are velocities in the unfractured rock.

In order to use Figure 9 to find the crack density parameter ε (and hence the initial damage D_o) from the seismic velocities ($\bar{v}_P$ and $\bar{v}_S$) at each test site, we need to know the un-fractured velocities (v_P and v_S) for the source rock at each site (the schist and the gneiss). These we estimate using the ultrasonic velocities measured in laboratory samples of each rock type by New England Research (NER).

For the schist source rock from the dry (un-frozen) site, NER measured P and S wave velocities under dry, saturated, and frozen conditions, at confining pressures ranging from 5 to 70 MPa. Table 2 summarizes the values at 5 and at 70 MPa - values at intermediate pressures vary monotonically between these limits.

Table 2. Ultrasonic data for schist source rock from the dry unfrozen site.

	P (MPa)	$\bar{v}_P$ (m/s)	$\bar{v}_S$ (m/s)	ν	$v_P{}^*$ (m/s)	$v_S{}^*$ (m/s)
Dry	5	4150	2800	0.082	5253	3294
	70	4750	3200	0.085	5723	3556
Saturated	5	5200	3000	0.25	5306	3261
	70	5450	3400	0.18	5561	3579
Frozen (-8C)	5	5800	3700	0.16		
	70	5700	3700	0.14		

*Unfractured reference velocities v_P and v_S found using ε_P and ε_S from Table 2.

The last two columns of Table 2 contain estimates of the un-fractured P and S wave velocities that were made using the calculations summarized in Table 2. In Table 2, values of $\frac{\bar{v}_P(sat.)}{\bar{v}_P(dry)}$ and $\frac{\bar{v}_S(sat.)}{\bar{v}_S(dry)}$ are calculated from the data in Table 1. Note that $\frac{\bar{v}_P(sat.)}{\bar{v}_P(dry)} = \frac{\bar{v}_P(sat.)/v_P}{\bar{v}_P(dry)/v_P}$ and that $\frac{\bar{v}_S(sat.)}{\bar{v}_S(dry)} = \frac{\bar{v}_S(sat.)/v_S}{\bar{v}_S(dry)/v_S}$ and that the ratios on the right hand side of these equations can be found as a function of ε in Figure 9 and are plotted explicitly in Figure 16. The values of ε in Table 2 were found using Figure 16 as indicated on the figure. Once ε was determined, the ratios $\bar{v}/v$ were found from Figure 9 and appear in the last four columns of Table 2. These ratios were used together with the measured seismic velocities to calculate the un-fractured velocities in the gneiss samples, which are give in the last two columns of Table 2. Note that the un-fractured velocities found by this method are very similar to the velocities measure in the frozen samples. This observation supports our assumption that ice immobilizes the fractures.

Table 3. Ultrasonic velocity ratios used to find fracture parameter ε in gneiss lab samples.

P (MPa)	$\frac{\bar{v}_P(sat.)}{\bar{v}_P(dry)}$	$\frac{\bar{v}_S(sat.)}{\bar{v}_S(dry)}$	ε_P	ε_S	$\frac{\bar{v}_P}{v_P}$ (dry)	$\frac{\bar{v}_P}{v_P}$ (sat.)	$\frac{\bar{v}_S}{v_S}$ (dry)	$\frac{\bar{v}_S}{v_S}$ (sat.)
5	1.25	1.07	0.18	0.16	0.79	0.98	0.85	0.92
70	1.15	1.06	0.13	0.15	0.83	0.98	0.90	0.95

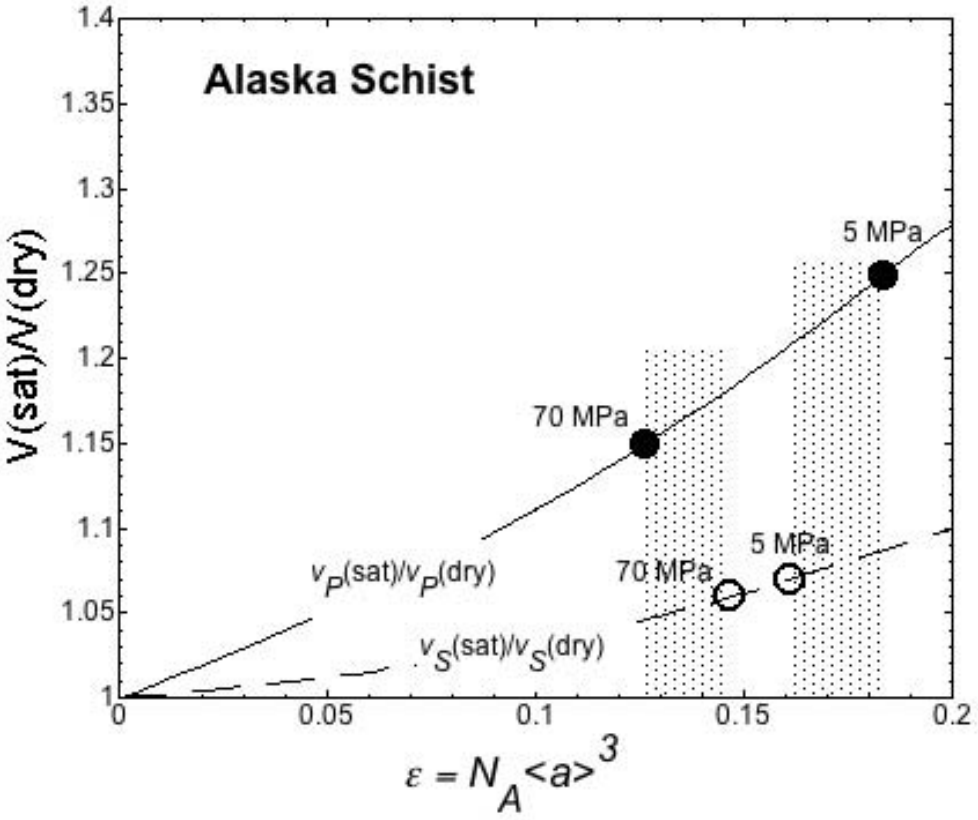

Figure 16. The ratio of saturated to dry velocities as a function of the crack parameter ε. The curves were calculated from Figure 2. The points are ratios of the ultrasonic data for schist from Table 2. Note the decrease in crack parameter as confining pressure closes cracks.

For the gneiss source rock from the frozen site, NER measured P and S wave velocities under saturated and frozen conditions, also at confining pressures ranging from 5 to 70 MPa. Table 4 summarizes the values at 5 and at 70 MPa - values at intermediate pressures vary monotonically between these limits.

Table 4. Ultrasonic velocities for gneiss source rock from the frozen site.

	P (MPa)	$\overline{v}_P$ (m/s)	$\overline{v}_S$ (m/s)	ν
Saturated	5	5450	3050	0.27
	70	5550	3200	0.25
Frozen (-8C)	5	5800	3400	0.24
	70	5800	3450	0.23

Since no measurements were made under dry conditions, we can not use the same method we used to estimate the un-fractured velocities in the schist. However, based on the results for the schist, we can assume that the frozen velocities are a reasonable approximation to the un-fractured velocities.

Having estimated the un-fractured velocities v_P and v_S for both source rocks, it is now possible to estimated the fracture parameter at each test site. The seismic field velocities and implied fracture parameters at each site are summarized in Table 5.

Table 5. Ultrasonic velocities for schist source rock from the dry unfrozen site.

	$\bar{v}_P$ (m/s)	$\bar{v}_S$ (m/s)	ν	$\frac{\bar{v}_P}{v_P}$	$\frac{\bar{v}_S}{v_S}$	ε_P	ε_S	$\langle\varepsilon\rangle$	$\langle D_o\rangle$
Unfrozed Site	2700	1700	0.17	0.47	0.46	0.41	0.45	0.43	1.80
Frozen Site	3800	2400	0.17	0.66	0.65	0.28	0.35	0.31	1.30

Note that for both P and S waves, the fracture parameter ε, and the equivalent initial damage D_o, is larger at the unfrozen site, consistent with the hypothesis that ice reduces the fracture density in the source rock. When these values of D_o are used in the Johnson and Sammis (2001) source model, the unfrozen site has a larger elastic radius and lower corner frequency than the frozen site, as observed in the Alaska frozen rock experiment.

4. RESULTS AND DISCUSSION

Laboratory studies of the effects of ice on the material properties of rock find that it increases the elastic stiffness and strength. These effects are observed to be both temperature and strain-rate dependent, with the stiffness and strength increasing at lower temperatures and higher strain-rates. These observations can be explained using a micromechanical damage mechanics where the primary effect of ice in the cracks is to decrease the crack density and increase the coefficient of sliding friction. When applied to a field experiment in which identical explosions were detonated in frozen and unfrozen rock, the suppression of damage by ice in the cracks explains the observation of a smaller elastic radius at the frozen site.

5. CONCLUSIONS

Frozen rock can have a significant effect on seismic coupling of underground nuclear explosions detonated in the permafrost layer. By suppressing fracturing in the non-linear source region, such explosions have a smaller elastic radius than those detonated in unfrozen rock. They radiate more high frequency energy and appear to have a lower yield.

REFERENCES

Ashby, M. F. and C. G. Sammis (1990) The Damage Mechanics of Brittle Solids in Compression, *Pure appl. Geophys*: 133, 489-521.

Bowden, F. P. and D. Tabor. (1950) *The Friction and Lubrication of Solids. Part I,* Clarenden Press, Oxford.

Bowden, F. P. and D. Tabor. (1964) *The Friction and Lubrication of Solids. Part II,* Clarenden Press, Oxford.

Denny, M. D. (1994). Introduction and Highlights, in *Proceedings of the Symposium on the Non-Proliferation Experiment (NPE): Results and Implications for Test Ban Treaties*, M. D. Denny (editor), CONF-9404100, Department of Energy.

Dieterich, J.H., and B.D. Kilgore (1996), Imaging surface contacts: Power law contact distributions and contact stresses in quartz, calcite, glass, and acrylic plastic, *Tectonophysics*, *256*, 219-239.

Duval, P., M. F. Ashby, and I. Anderman (1983), Rate controlling processes in the creep of polycrystalline ice, *J. Phys. Chem.,* 87, 4066-4074.

Frost, H.J. and M.F. Ashby (1982). *Deformation-Mechanism Maps*, Pergamon Press, New York.

Glenn, L. A. (1993). Energy-density effects on seismic decoupling, *J. Geophys. Res.*: 98, 1933-1942.

Glenn, L. A. and P. Goldstein (1994). Seismic decoupling with chemical and nuclear explosions in salt, *J. Geophys. Res.*: 99, 11,723-11,730.

Goodman, D. J., H. J. Frost, and M. F. Ashby (1981), The plasticity of polycrystalline ice, *Phil. Mag. A*, 43, 665-695.

Johnson, L. R. (1993). Wave propagation near explosive sources, PL-TR-93-2118, Phillips Laboratory, 22 pp.

Johnson, L. R. and C. G. Sammis (2001). Effects of rock damage on seismic waves generated by explosions, *Pure Appl. Geophys.*: 158, 1869-1908.

King, D. S., B. E. Freeman, D. D. Eilers, and J. D. Johnson (1989). The effective yield of a nuclear explosion in a small cavity in geologic material: enhanced coupling revisited, *J. Geophys. Res.:* 94, 12,375-12,385.

Mellor, M. (1973). Mechanical properties of rocks at low temperatures, *Second International Conference on Permafrost,* National Academy of Sciences, Washington, D.C., 334-343.

O'Connell, R.J. and B. Budiansky (1974). Seismic velocities in dry and saturated cracked solids, *J. Geophys. Res.:* 79, 5412-5426.

Rimer, N., J. L. Stevens, J. R. Murphy, and G. G. Kocharyan (1998) Estimating seismic characteristics of explosions in hard rock using a micro-mechanical damage model, p. 392-400 in Proceedings of the 20th Annual Seismic Research Symposium on Monitoring a Comprehensive Test Ban Treaty, J. Fantroy, D. Heatley, J. Warren, F. Chavez, and C. Meade (eds), Department of Defense and U.S. Department of Energy.

Rodean, H.C. (1971), Nuclear-Explosion Seismology, U.S. Atomic Energy Commission, TID-25572, 156 pp.

Sammis, C. G. (1998) Acoustic fluidization in the damage regime of explosions in crystalline rock, p. 417-421 in Proceedings of the 20th Annual Seismic Research Symposium on Monitoring a Comprehensive Test Ban Treaty, J. Fantroy, D. Heatley, J. Warren, F. Chavez, and C. Meade (eds), Department of Defense and U.S. Department of Energy.

Sammis, C.G. and R.L. Biegel (2004). "Mechanics of strengthening in crystalline rock at low temperatures: a preliminary assessment," in *Proceedings of the 26th Seismic Research Review: Trends in Nuclear Explosion Monitoring*, Orlando, FL.

Sammis, C.G. and R.L. Biegel (2005). "Seismic radiation from explosions in frozen crystalline rock," in *Proceedings of the 27th Seismic Research Review Ground-Based Nuclear Explosion Monitoring Technologies*, Rancho Mirage, CA.

Stevens, J.L., C.E. Baker, H. Xu, T.J. Bennett, N. Rimer, and S.M. Day (2003) The physical basis of Lg generation by explosion sources, Proceedings of the 25th Seismic Research Review, p456.

Stevens, J.L., N. Rimer, H. Xu, J.R. Murphy, C.E. Baker, G.G. Kocharyan, B.A. Ivanov and S.M. Day (2001) Nearfield and regional modeling of explosions at the Degelen test site, Proceedings of the 23th Seismic Research Review, p540.